PLASTIC STRAIN AND STRAIN GRADIENTS AT VERY SMALL INDENTATION DEPTHS

N. I. TYMIAK[1], D. E. KRAMER[1], D. F. BAHR[1], T. J. WYROBEK[2] and W. W. GERBERICH[1]†

[1]Department of Chemical Engineering and Materials Science, University of Minnesota, 151 Amundson Hall, 421 Washington Avenue, S.E., Minneapolis, MN 55455-0132, USA and [2]Hysitron Inc., Minneapolis, MN 55349, USA

Abstract—Plastic strains and their respective strain gradients produced by nanoindentation have been theoretically interpreted and experimentally measured at shallow indentation depths. Existing data for ⟨100⟩ tungsten with four different conical tip radii varying from 85 to 5000 nm and new data for four conical tips (R = 0.5 to 20 μm) into ⟨100⟩ aluminum are presented. Theoretical results based on geometrically necessary dislocations and semi-empirical experimental continuum calculations are compared for spherical and wedge indenters. For a sharp wedge, both experimental continuum based and theoretical geometrical approaches suggest strain gradient decreasing with the increasing indentation depth, δ. In contrast, theoretical geometrical analysis for a spherical contact yields a depth independent strain gradient proportional to $1/R$ and continuum calculations suggest a slight increase of a strain gradient proportional to $\delta^{1/4}/R^{3/4}$. Both single crystals exhibit about a factor of two decrease in hardness with increasing depth, irrespective of either increasing or decreasing average strain gradients. Implications to strain gradient plasticity and indentation size effect interpretations at very shallow depths are discussed. © 2001 Acta Materialia Inc. Published by Elsevier Science Ltd. All rights reserved.

Keywords: Hardness; Dislocations; Yield phenomena; Metallic; Atomic force microscopy (AFM)

1. INTRODUCTION

Theoretical and practical aspects of nanoindentation at very small scales has come under increased scrutiny. On the mechanics side, theories of strain gradient plasticity can be evaluated experimentally [1–3]. One such approach uses experiments at different depths to assess the indentation size effect (ISE) where the hardness at small depths is much greater than at deeper ones. On the practical side, an understanding of hardness, flow strength, friction and wear appropriate to design at very small volumes is essential for MEMS and microelectronic devices.

Perhaps the most interesting scale aspect is that indentation hardness can drop by more than a factor of two [3] with increasing depth and this depth dependence appears to be more accentuated in single crystals than polycrystals. Whether this is strictly due to the difference in the initial dislocation density and/or number of sources is still under investigation. The important aspect to mechanics theory is that the findings are internally consistent with strain gradient plasticity laws. For our purposes, in dealing with very thin films or other small volumes, we often deal with penetration depths of a few to several hundred nanometers. This gave us reason to further examine such models since the experimental basis involved data no shallower than 160 nm [1–3]. As Gao and Nix [3] have already shown, the strain gradient, χ, is proportional to $1/\delta$ where δ is the depth of penetration of perfectly sharp wedge-shaped tips.‡ See Fig. 1. Upon the assumption that a geometrically necessary dislocation density, ρ^G, controls plastic strain, ϵ_p, at small scales, one has $\epsilon_p \propto \chi a \propto \frac{\delta}{a}$ for sharp, constant-angle indenters like a Berkovich or Vickers. Conversely, at the very shallow depths of interest to this study, neither of these tips is perfectly sharp giving meaning to the consideration of spherical tips. A number of studies including Tabor's [4] original estimate of ϵ_p for spherical tips give strain proportional to the ratio of the contact radius, a, to tip radius, R. Further, since Hertzian theory or geometry would

---

† To whom all correspondence should be addressed. Tel.: +1-612-625-1313; fax: +1-612-626-7246.
E-mail address: wgerb@tc.umn.edu (W. W. Gerberich)

‡ We use δ here as opposed to h, commonly used for film thickness, as the indentation size effect can have important ramifications to thin films.

(a)

(b)

$$\varepsilon_p = \frac{\delta}{a} \propto \chi a \qquad \chi = \frac{\delta}{a^2} = \frac{\tan\theta}{a}$$
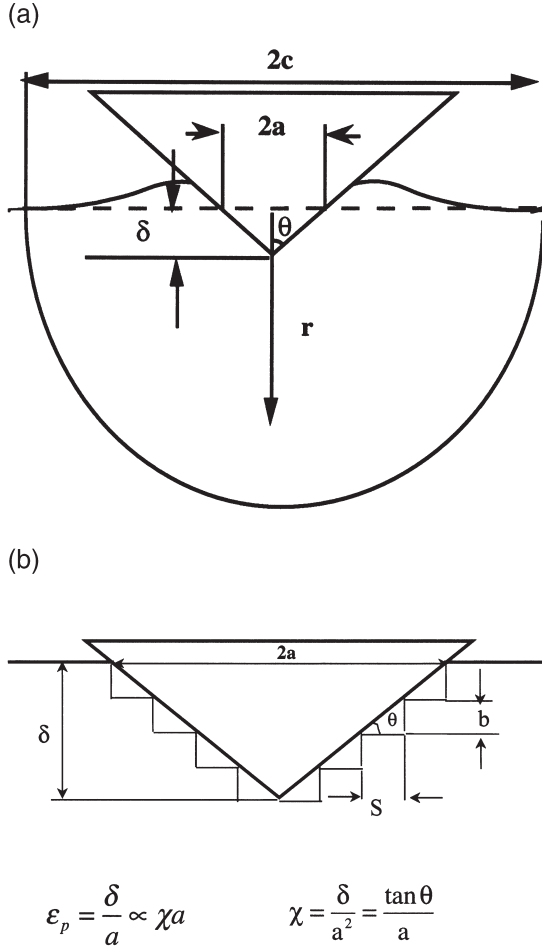
Fig. 1. (a) Schematic of an elastic–plastic wedge contact. (b) Schematic of geometrically-necessary dislocation geometry for a perfectly-sharp rigid wedge indentation (after Gao and Nix [3]).

have $a \propto \sqrt{R\delta}$, it is seen that strain is proportional to $(\delta/R)^{1/2}$. Note for a constant angle indenter that δ/a is constant giving plastic strain to be independent of depth. This characteristic difference in plastic strain dependency in wedge-shaped indenters being proportional† to $(\delta/R)^{1/2}$ at very shallow depths (as it is in spherical tips) and δ/a at larger depths requires attention. Basic questions are first whether or not dislocation densities and their corresponding strain gradients differ substantially in character at shallow versus deeper depths of penetration. This further suggests a second question as to whether an indentation size effect (ISE) is expected for very shallow penetrations where plastic strain increases with depth. Finally, it seems that any ISE found at very shallow depths might require a different mechanistically-based law.

---

† We recognize here that with the given definition of a that $(\delta/R)^{1/2}$ is still δ/a but this is not constant for spherical tips as it is for perfectly sharp ones. With R a constant, it is easier to see that $(\delta/R)^{1/2}$ varies at shallow depths.

To investigate this further we decided to evaluate shallow spherical indentations with various contact radii. These were conducted with a range of tip sizes so that in as many cases as possible spherical contacts were being evaluated.

An objective was to evaluate hardness vs depth variations starting from very shallow depths up to a transition between spherical and wedge contacts. Comparison between a spherical and wedge contact would require an appropriate definition of a strain gradient for a spherical contact. As defined for a wedge [3], strain gradient in fact represents a ratio of plastic strain with respect to a contact indentation radius. Here, a contact radius can be regarded as "a gage length" corresponding to a total extent of plastic deformation. With such a definition strain gradient denotes change of plastic strain with the changing extent of plastic deformation rather than spatial variation of plastic strain. Note also that this type of a model based on discrete dislocation arrangement defines resulting strain gradient in terms of continuum measures such as indentation depth and indentation contact radius. With the above, it seems appropriate to define strain gradient for a spherical contact also based on continuum quantities. As was utilized for the wedge contact, contact radius may be regarded as a "plastic gage length" corresponding to the total extent of plastic deformation. Alternative choices for plastic gage length will be considered later. To obtain an accurate measure of plastic strain, it is necessary to deconvolute a plastic displacement from a total elastic–plastic indentation depth. Such a possibility exists for single crystals exhibiting yield excursion phenomena, previously found in Fe3wt%Si, Mo and Cu [5, 11], Ni [6], W [7–11] and Au [12–14]. An example of such an excursion is shown in Fig. 2. Yield excursions are associated with discrete events
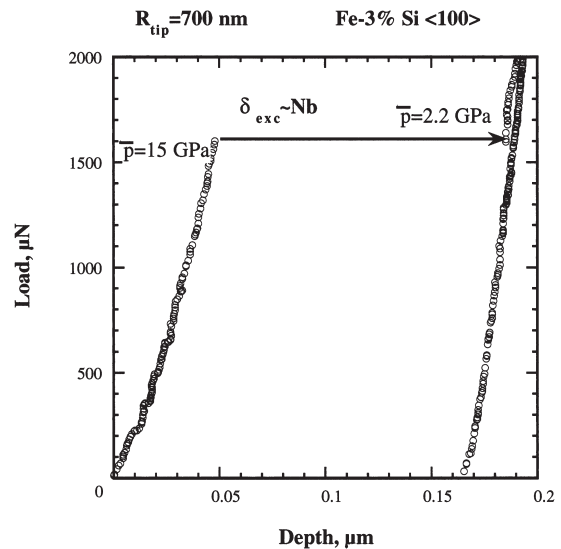

Fig. 2. Load–depth curve of an indentation into the ⟨100⟩ face of an Fe–3wt%Si single crystal. The initial portion follows elastic contact theory.

of dislocation nucleation and evolution under indentation contact [5–15]. For some metals there is clear evidence of the effects of oxide or surface layer fracture events and associated dislocation breakthrough to a free surface [5–15]. Despite the complexity of the processes leading to a yield excursion, it is clear that such an excursion is associated with an instantaneous irreversible plastic deformation. Thus, the extent of an excursion gives a clear measure of plastic deformation. Such a measure can possibly be used in continuum based approaches, leaving out consideration of the nature of discrete events and mechanisms leading to an excursion. Associating such a plastic displacement with a gage length or appropriate size scales allows both a plastic strain and a plastic strain gradient to be estimated. While the state of stress and strain just after such an event may be a special case, it is a very important one associated with the earliest stages of plasticity under contact, of importance to tribological issues and small volumes. With that caveat, we proceeded to the question of what represents an appropriate length scale(s) for assessing plastic strain. Three possibilities arose—the depth of penetration, δ; the contact radius, a; and the plastic zone radius, c. As some authors [16, 17] have used $d\delta/\delta$ as a reasonable measure of strain this was considered briefly. However, for small depths of penetration where δ_{exc} was as much as 70% of the total depth, strains of 0.7 seemed high compared to Tabor's [4] and others [18, 19] original estimates and so we rejected this. The possibilities of contact radius and plastic zone, however, seemed to be natural choices. For the first one can consider prismatic punching so that if dislocations are punched out on a glide cylinder then the glide cylinder would have a dimension equal to the contact diameter of the punch. On the other hand, it is well known that plastic pile-up occurs around indentations into most single crystals [5–14]. Thus indentation displacement is partly accommodated by material displaced above an initial zero plane. This is in contrast to the geometrically necessary configuration utilized by a wedge-indentation modeling which assumes no pile-up. With the above, plastic zone radius, c, may be a better gage length parameter for experimentally determining the average strain gradient in the deforming volume. We use both a and c as possible length parameters for the strain gradient in the following discussion. Replacing derivatives with respect to a plastic gage length by a simple division such as e.g. $\partial \epsilon/\partial c$ by simple division ϵ/c would give a relative average measure of plastic strain increase with respect to a total extent of plastic deformation. Such a measure will be referred to as "plastic strain gradient" for experimental evaluations.

With this background, the following addresses theoretically and semi-empirically the strain gradients under sharp wedge and spherical contacts. We then describe the analysis of strain gradients from single crystal nanoindentation experiments previously presented, and describe a new set of experiments conducted on an aluminum single crystal. Discussion of how this might be used to rationalize an ISE at very shallow depths is then considered.

2. THEORY

Here, we only briefly review the strain gradient aspects of the sharp-angled indenter already extensively discussed [3]. We then consider the strain gradient associated with a spherical indentation which by necessity is on a more tenuous basis. In both cases, we consider and compare plastic strain gradient assessment using (i) experimental continuum based values averaged over the plastic zone and (ii) theoretical values based on geometrically necessary dislocations.

2.1. Sharp, angled indenters

For perfectly sharp, angled indenters we take the geometric estimate of $\chi = tg(\theta)/a$ as shown in Fig. 1(a). It is useful to compare this geometric estimate of χ to an average continuum value. For Johnson's cavity model which applies to a wedge, it was previously shown that the plastic strain gradient could be given by [20]

$$\frac{d\epsilon_{\text{p}}}{dc} \simeq -6(1-\nu)\frac{\sigma_{\text{ys}}}{E}\frac{c^2}{r^3}.$$ (1)

The corresponding schematic of an elastic–plastic wedge indentation is shown in Fig. 1(a). An average plastic strain gradient may be obtained from equation (1) by integrating between the indenter tip and the plastic zone boundary. This gives

$$\left|\overline{\frac{d\epsilon_{\text{p}}}{dc}}\right| = -6(1-\nu)$$
$$\times \frac{\sigma_{\text{ys}}c}{E}\int_{\delta}^{c}\frac{dr}{r^3} \simeq \frac{12(1-\nu)c}{\delta a}\cdot\frac{\sigma_{\text{ys}}}{E};$$ (2a)
$$c \gg \delta, \delta = a\tan(\theta)$$

Based on the wedge geometry, a cut-off is given by $\delta = a\tan(\theta)$. It should be cautioned that using equation (2a) requires an exact value of indenter included angle which may vary at different depths. For the Vickers indenter utilized by Harvey *et al*. [19], the included angle was 13.6° (rather than the expected 19°) at shallow indentation depth. This would give a cut-off of $\delta \sim 0.24a \sim a/4$. By using an observed, c/a ratio of three determined from some previous contacts [20], equation (2a) simplifies to

$$\left|\overline{\frac{d\epsilon_{\text{p}}}{dc}}\right| \simeq \frac{144(1-\nu)}{a}\cdot\frac{\sigma_{\text{ys}}}{E}$$ (2b)

This mean value below the tip may be compared with

the wedge indentation of tungsten by using a flow stress that was determined previously for *W* to be 0.86 GPa [9]. A method of yield stress determination is addressed briefly in the Results and Discussion. With $E = 400$ GPa, this gives

$$\left|\overline{\frac{d\epsilon_p}{dc}}\right| \approx \chi = \frac{0.232}{a}. \tag{3}$$

A geometrical gradient value may be calculated as shown in Fig. 1(b). For a 13.6° wedge, it would give $\chi_{geometric}^{wedge} \approx 0.24/a$. This compares favorably with $\chi_{continuum}^{wedge} \approx 0.232/a$ as given by equation (3).

2.2. Spherical indenters

As pointed out by Johnson [22], the slip-line field being curvilinear coupled with complications of the free surface changing, make elastic–plastic solutions intractable. He reports no known exact slip-line solutions for indenters with curved surfaces. For that reason we resort to estimating strain gradients as average strain values normalized on some length parameter, e.g. *a* or *c*. For geometric considerations we use Fig. 3 for the interpretation of the strain gradient at a spherical contact, analogous to the wedge contact of Fig. 1. In the following then we consider Tabor's estimate, a geometrically-necessary estimate and a geometric one.

First consider Tabor's estimate of strain given by [4]

$$\epsilon_p \approx 0.2\left(\frac{a}{R}\right). \tag{4}$$

Normalizing on the contact radius, *a*, as the gage length gives

$$\chi \approx \frac{1}{5R}. \tag{5}$$

A similar result is obtained from geometrically-necessary dislocations treating a spherical contact analogously to shear loops about a second phase particle.
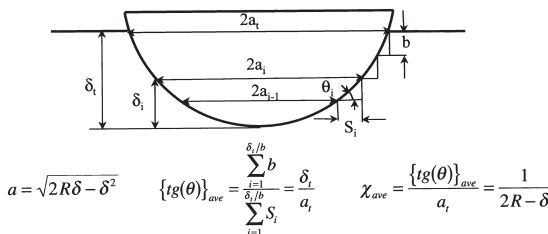
As schematically shown in Fig. 4, this gives a local strain of

$$\epsilon_p = \frac{Nb}{2a} \tag{6}$$

where *N* would be the number of shear loops consistent with *Nb* displacement. Differentiating this with respect to the contact radius gives

$$\chi \approx \left|\frac{\partial \epsilon_p}{\partial a}\right| \approx \frac{\delta_{plastic}}{2a^2} \tag{7}$$

where we consider the gradient as positive. Since for a geometrical contact of a sphere, $a^2 \approx 2\delta R$, elimination of δ gives

$$\chi \approx \frac{1}{4R}. \tag{8}$$

Alternatively, an arrangement of geometrically necessary dislocations accommodating a spherical indentation may be modeled in a similar way as utilized for a wedge indentation [3]. This involves circular loops with the Burgers vectors normal to the indented surface as shown in Figs 1 and 3 for wedge and spherical contacts, respectively. Note that in contrast to a constant angle wedge, the *b/S* ratio is not constant for a sphere. Defining a characteristic angle θ representing plastic strain and the associated strain gradient, χ_i, yields

$$tg\theta_i = \frac{b}{S_i}; \tag{9}$$

$$\chi_i = \frac{tg\theta_i}{a_i}; \tag{10}$$

$$a = \sqrt{2R\delta - \delta^2} \qquad \{tg(\theta)\}_{ave} = \frac{\sum_{i=1}^{\delta_t/b} b}{\sum_{i=1}^{\delta_t/b} S_i} = \frac{\delta_t}{a_t} \qquad \chi_{ave} = \frac{\{tg(\theta)\}_{ave}}{a_t} = \frac{1}{2R-\delta}$$

Fig. 3. Schematic of geometrically-necessary dislocation geometry for a rigid spherical indentation.

An Average Strain Gradient at "Plasticity Onset"

Geometrically Necessary (Ashby)

$$\varepsilon_p = \frac{Nb}{d}$$

$$\bar{\varepsilon}_p = \frac{Nb}{2a}$$

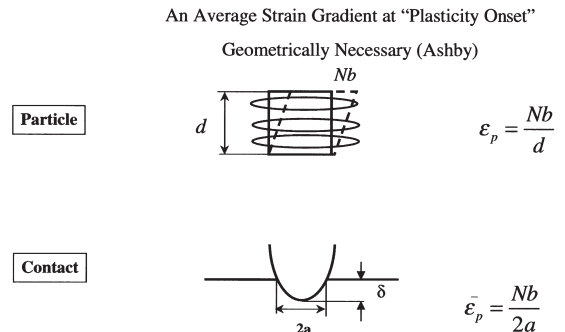Fig. 4. Analogous treatment of particles and spherical contacts nucleating dislocation loops.

$$\{tg(\theta)\}_{\text{ave}} = \frac{\sum\limits_{i=1}^{\delta_t/b} b}{\sum\limits_{i=1}^{\delta_t/b} S_i} = \frac{\delta_t}{a_t}. \tag{11}$$

A first order estimate of the corresponding average strain gradient values may be as follows:

$$\chi_{\text{ave}} = \frac{\{tg(\theta)\}_{\text{ave}}}{a_i} = \frac{1}{2R-\delta}. \tag{12a}$$

Here, we utilize

$$a = \sqrt{2R\delta-\delta^2} \tag{13}$$

For $\delta \ll R$ equation (12a) reduces to

$$\chi_{\text{ave}} \approx \frac{1}{2R}. \tag{12b}$$

Note that equation (11) underestimates an average value of the plastic strain as compared to that given by

$$\frac{1}{\delta_t/b}\sum_{i=1}^{\delta_t/b}\frac{b}{S_i}$$

This asymptotically approaches $\chi'_{\text{ave}} = 1/R$.

As follows from equations (9) and (10), both strain and strain gradient attain their maximum values at $a_i = a_t$. Figure 5 shows $\chi_{\text{max}}(a)$ dependencies calculated for different tip radii as based on geometry of
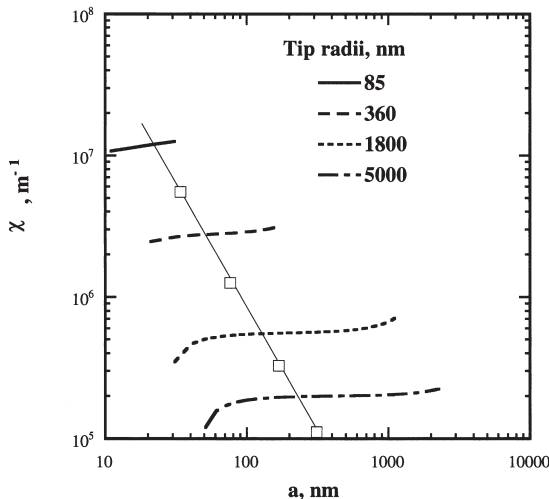
a spherical contact. Calculations were carried out for indentation depths up to the transition between spherical and conical regions. It appears that strain gradient increases slightly with increasing penetration remaining very close to $1/R$ for all indenter tip radii. Note that the average value from equation (12a) is identical to analytically using the incremental form of the contact shown in Fig. 3 and integrating to find the strain. First,

$$d\epsilon = \frac{d\delta}{2a} = \frac{d\delta}{2[2\delta R]^{1/2}}. \tag{14}$$

Integration gives

$$\epsilon = \frac{1}{2\sqrt{2R}}\int_0^{\delta_{max}}\frac{d\delta}{\delta^{1/2}} = \frac{1}{\sqrt{2}}\sqrt{\frac{\delta_{max}}{R}} \tag{15}$$

Since $\delta_{\text{max}} \simeq a^2/2R$, inserting this into equation (15) and normalizing on a gives

$$\chi \simeq \frac{1}{2R}. \tag{16}$$

The comparison of equation (16) to the incremental calculation is shown in Fig. 5. Since this integrated form of incremental contact is the same as the average gradient summed along the sphere profile, we believe the more appropriate geometric measure of χ at maximum depth is given by equation (16). All of these, along with a hardening analysis by Matthews, are summarized in Table 1. Here, it is seen that normalization on a as a length scale yields strain gradients ranging from about $1/2R$ to $1/5R$ whereas the sharp wedge gave χ as δ/a^2. This different dependence of χ on depth, particularly at very shallow depths is examined in the following.

Fig. 5. Strain gradients from spherical geometry considerations for four different tip radii.

Table 1. Strain gradients with a normalization[a]

Investigator	Strain, ϵ	Strain gradient, $\bar{\chi}$
Tabor	$\epsilon = 0.2\left(\dfrac{a}{R}\right)$	$\bar{\chi} = \dfrac{\epsilon}{a} = \dfrac{1}{5R}$
Matthews[b] (hardening)	$\epsilon = \dfrac{a}{2R}\left(\dfrac{2n}{2n+1}\right)^{2(n-1)}$	$\dfrac{1}{2R} < \bar{\chi} < \dfrac{1}{5.4R}$
Ashby (geometrically necessary)	$\epsilon = \dfrac{Nb}{2a}$	$\bar{\chi} = \dfrac{Nb}{2a^2} = \dfrac{\delta}{4\delta R} = \dfrac{1}{4R}$
Geometry	$\bar{\epsilon} = tg\bar{\theta} = \dfrac{\delta}{a}$	$\bar{\chi} = \dfrac{\delta}{a^2} = \dfrac{1}{2R}$

[a] a = contact radius; R = tip radius.

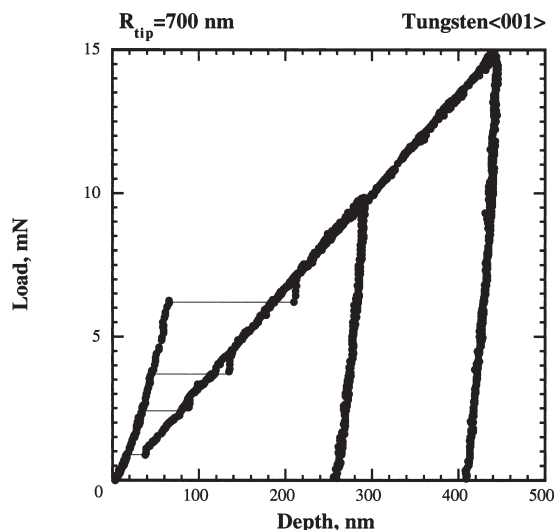[b] $\sigma = \sigma_{\text{ys}}\left(\dfrac{\epsilon}{\epsilon_{\text{ys}}}\right)^{1/n}$.

Fig. 6. Displacement excursions during plastic yielding at a 700 nm tip driven into ⟨100⟩ tungsten.

3. EXPERIMENTAL

A simple experimental approach, as alluded to in Fig. 4, is to use the plastic strain that can be unambiguously associated with a displacement excursion like that shown in Fig. 2. Typical excursions in other materials, here W and NiAl, are shown for comparison in Figs 6 and 7. Note first a wide range of loads at which excursions occur. Reasons for such variations in yield point loads are currently being addressed in a forthcoming paper [23]. In such excursions, giving large differences in δ, the important point is that a range of strains as represented by equation (15) can be generated by a single tip radius. A summary of such excursions for four tip radii is
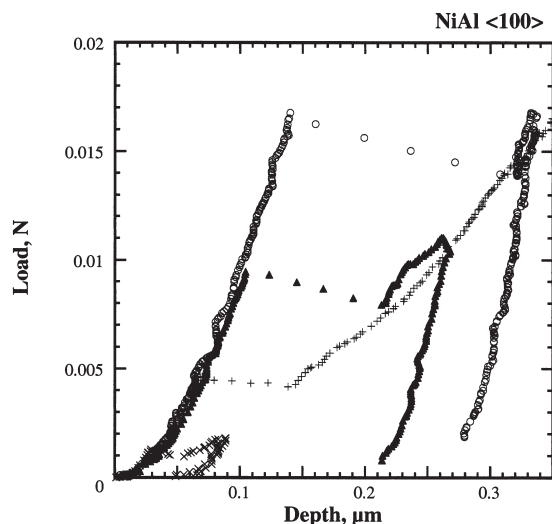
shown in Fig. 8. While strain gradients were calculated from the format outlined in Fig. 4 for several materials, we would rather utilize directly measured plastic zone diameters, contact radii and displacements or displacement excursions, for the experimental evaluation. For confirmation then, we chose an ⟨001⟩ aluminum single crystal and four 90° conical tips ranging from submicron to several microns radii of curvature. Indenter tip imaging with an ultra sharp silicon grating TGT01 and Hertzian analysis of elastic indentation into fused quartz have been utilized for indenter tip radii assessment. Obtained values of 0.47, 0.98, 5.45 and 18.1 μm will be further referred to as nominal indenter tip radii of 0.5, 1, 5 and 20 μm. Indentation tests were then performed with the Hysitron Triboscope, an AFM attachment providing both indentation and in-situ imaging capabilities. Smooth areas with surface roughness below 10 nm were chosen for indentation experiments. For the two sharper tips, evaluation has been extended to penetration depths beyond the spherical region. To account for indentation induced pile-up, hardness values were assessed based on the contact radii obtained from imaging of residual indentation impressions. Indentation induced plastic zone radii, *c*, were also determined from post-indentation imaging of indented areas.

4. RESULTS AND DISCUSSION

Initial comparisons were made for plastic zones, contact radius, plastic strains and strain gradients as taken from previous studies [9, 11]. With excursions given in Figs 6–8, strain and strain gradients were calculated using the plastic zone size as a length scale parameter. As shown in detail elsewhere [21], this plastic zone can be calculated from

Fig. 7. Displacement excursions during plastic yielding at a 1 μm tip driven into ⟨100⟩ NiAl.
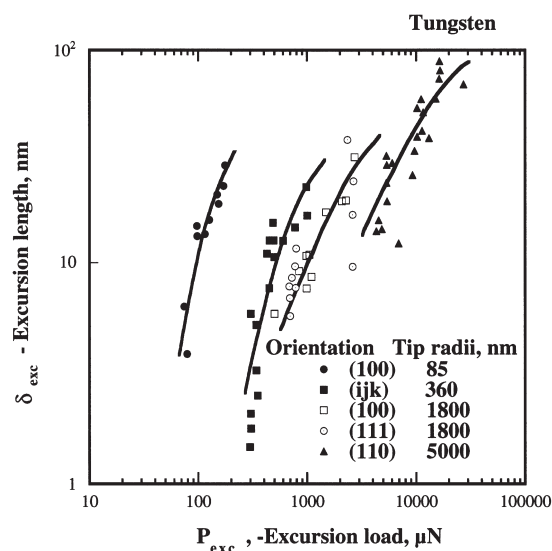

Fig. 8. Displacement excursions as a function of yield load and indentation tip radius for various orientations of tungsten single crystals (after Gerberich *et al.* [11]).

$$c = \sqrt{\frac{3P}{2\pi\sigma_{\text{ys}}}} \qquad (17)$$

where σ_{ys} is the far field tensile yield strength and P is the load. The current study relied on yield stress determined from previous indentation experiments with similar indenter tip radii where the curve fit of equation (17) over an extended depth range was used. We do realize that possible errors could be introduced with such an approach but believe this may be used as a good estimate. Note that such errors will not change values of c appreciably because of the square root dependence. Even if such errors were introduced, the dependence shown in Figs 9 and 11 would not change qualitatively. A summary of all of the $\langle 100 \rangle$ W single crystal data for the four tip radii is given in Table 2. From this table it is apparent that the plastic strains ($\sim\delta_{\text{exc}}/c$) increase from about 0.016 to 0.16 for these relatively shallow indents which have a total penetration depth range from 6 to 160 nm. For a typical 1 μm spherical tip, this would also be in rough agreement with Tabor's estimate, equation (4), for penetration depths of about 3 nm to 300 nm. With the above definition of strain, we further divide by c to obtain the "gradients" δ/c^2, also given in Table 2. These gradients are the data points shown as a function of displacement depth in Fig. 9. Here it is seen that the smaller radii tips have the largest strain gradients as might be expected for either imperfect wedge or spherically shaped tips at small penetration depths. However, there also appears to be a slight increase in strain gradient with increasing depth as well, the opposite of what would be expected if one were considering a perfect wedge shaped tip, e.g. equation (3).

Fig. 10. Hardness as a function of depth for four different tip radii into $\langle 100 \rangle$ aluminum.

A similar analysis was conducted for the $\langle 100 \rangle$ aluminum single crystal data except in this case all plastic zones and contact radii were directly measured by AFM. Here ϵ/c was also used for strain gradients. For the four conical indenters, these data as summarized in Table 3, represent those indentation depths less than or equal to the tip radius. For all the indenter tip radii, hardness increased with decreasing penetration depth and decreasing indenter tip radius as shown in Fig. 10. The strains and strain gradients, however, behaved quite differently compared to the $\langle 100 \rangle$ W. As seen by comparing Tables 2 and 3, the strains were nearly constant and the strain gradients decreased with increasing depth for the sharpest tip into aluminum. This is in contrast to both ϵ and χ increasing with increasing depth for tungsten. This difference is due to the relatively shallow penetration depths for the tungsten such that the tip contact remained close to spherical whereas for the aluminum the sharpest tip seemed to behave more like a wedge, particularly at penetrations with δ/R greater than 0.3†. Further confirmation of this is seen by examining the strains in aluminum where they were nearly constant with increasing depth for the 500 nm tip, slightly increasing for the 1000 nm tip, and increasing by a factor of three for the blunter 5 μm and 20 μm tips at increasing depths. Additional corroboration for aluminum is seen in the gradients which decrease sharply for the 500 nm tip with increasing depth as might be expected for a wedge. Contrary to this, the gradients were nearly constant with depth for the next
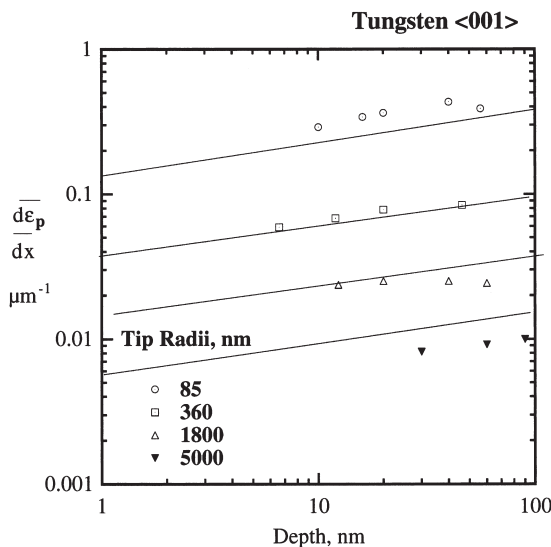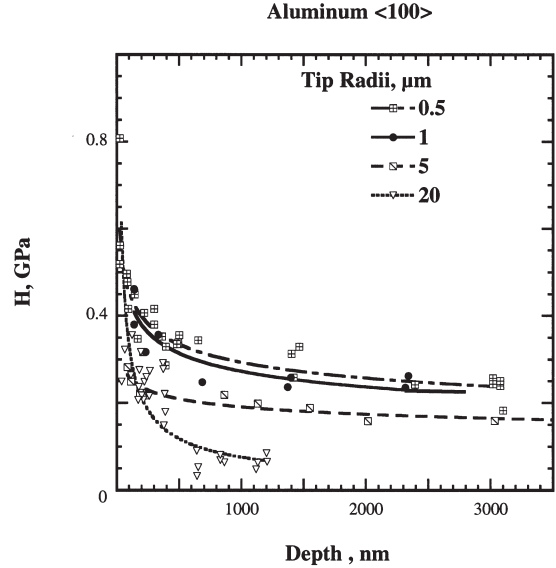

Fig. 9. Estimated strain gradients from Table 2 as a function of penetration depth for four different tip radii into $\langle 100 \rangle$ tungsten. Solid curves represent equation (23) with a size scale parameter of $\eta = 2$ μm.

---

† For a 90° cone, the transition between spherical and conical regions occurs at $\delta/R = (1-(1/\sqrt{2})) \approx 0.3$.

Table 2. Plastic strains[a], gradients[a] and hardnesses[a] for single crystal tungsten ⟨100⟩ using different tip radii

Tip radius (nm)	P (μN)	c^b (nm)	δ (nm)	a^c (nm)	c/a	ϵ	χ (μm^{-1})	H (GPa)
85	80	210	10	41.2	5.1	0.048	0.227	15
	90	224	16	52.2	4.3	0.071	0.319	10.5
	100	236	20	58.3	4.1	0.085	0.359	9.4
	140	279	40	82.5	3.4	0.149	0.514	6.7
	200	333	56	97.6	3.4	0.168	0.505	6.6
360	300	408	6.6	68.9	5.9	0.016	0.040	20
	400	472	12	92.9	5.1	0.025	0.054	14.8
	520	538	20	120	4.5	0.037	0.069	11.5
	1000	746	46	182	4.1	0.062	0.083	9.6
1800	700	620	12.4	211	2.9	0.020	0.032	5.0
	1000	746	20	268	2.8	0.027	0.036	4.4
	2000	1050	40	379	2.8	0.038	0.036	4.4
	3200	1330	60	465	2.9	0.045	0.034	4.7
5000	5000	1670	30	548	3.0	0.018	0.0107	5.3
	8000	2110	60	775	2.7	0.028	0.0135	4.2
	10,000	2360	90	949	2.5	0.038	0.0161	3.5
	17,000	3070	160	1265	2.4	0.052	0.0170	3.3

[a] For selected points on the solid curves in Fig. 8.
[b] From equation (17) with σ_{ys} = 860 MPa (Bahr *et al.* [9]).
[c] From $a \simeq \sqrt{2\delta R}$.

Table 3. Plastic strains, gradients and hardnesses for single crystal aluminum ⟨100⟩ using different tip radii

Tip radius (nm)	P (μN)	c^a (nm)	δ^b (nm)	a^a (nm)	c/a	ϵ	χ (μm^{-1})	H (GPa)
500	97	-	24	195	-	-	-	0.81
	97	-	26	234	-	-	-	0.56
	287	950	92	468	2.03	0.097	0.102	0.42
	483	1270	143	585	2.17	0.113	0.089	0.45
	483	1680	167	665	2.53	0.099	0.059	0.35
	671	1425	220	725	1.97	0.134	0.108	0.41
	671	1835	218	725	2.53	0.118	0.065	0.41
	671	2110	211	820	2.57	0.100	0.047	0.32
	966	2500	300	860	2.91	0.120	0.048	0.41
	966	2580	300	900	2.87	0.116	0.045	0.38
	1141	2500	364	1015	2.46	0.146	0.058	0.35
	1151	3085	394	1055	2.92	0.128	0.041	0.33
	1429	4120	500	1130	3.69	0.121	0.029	0.36
1000	495	1600	141	585	2.74	0.088	0.055	0.46
	497	1650	138	645	2.56	0.084	0.051	0.38
	720	2345	2333	850	2.75	0.099	0.042	0.32
	948	2675	333	920	2.91	0.124	0.047	0.36
5000	2500	4395	186	1400	3.14	0.042	0.0096	0.220
	3000	4930	236	1465	3.36	0.048	0.0097	0.220
	8000	8065	863	2730	2.95	0.107	0.013	0.218
	10 000	8900	1130	2600	3.43	0.126	0.015	0.199
	12 000	10 800	1548	2780	3.88	0.143	0.013	0.189
20 000	6000	9450	172	3040	3.11	0.0182	0.00193	0.207
	7000	9800	191	3160	3.10	0.0195	0.00199	0.223
	9950	11 250	261	3830	2.94	0.0232	0.00206	0.216
	13 980	12 770	376	5470	2.52	0.0273	0.00198	0.149
	13 980	12 990	389	4980	2.61	0.0299	0.00231	0.180
	20 000	16 440	640	8380	1.96	0.0389	0.00237	0.091
	25 000	16 550	830	9 880	1.67	0.0502	0.00303	0.082
	25 000	15 470	863	11 160	1.39	0.0558	0.00361	0.064
	25 000	15 030	830	10 740	1.40	0.0552	0.00367	0.069
	32 000	18 590	1130	12 680	1.47	0.0608	0.00327	0.063

[a] Directly imaged by AFM.
[b] For the deeper penetration depths here, it was assumed that $\delta_{plastic} \simeq \delta_{total}$ noting that in most cases it was more than 90% of the total.
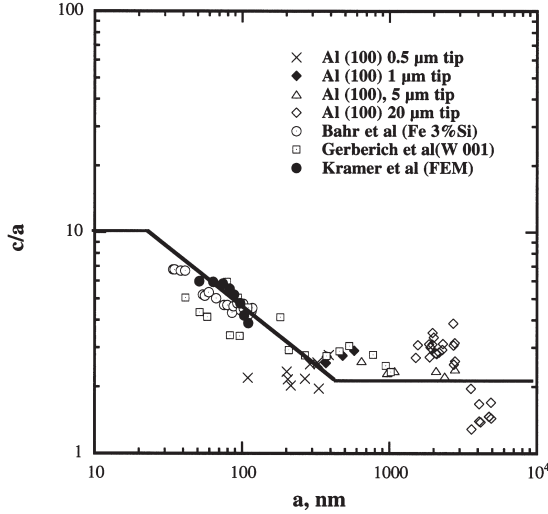
Fig. 11. Ratio of plastic zone to contact radii as a function of contact radius for three single crystal materials and an elastic–plastic finite element analysis.

two larger tips but clearly increasing with depth for the 20 μm tip. The situation thus evolves that for nearly all of the tungsten data, strains and gradients increased with depth while mixed behavior resulted in the sharpest tip behaving more wedge-like and the largest tips more spherical-like for aluminum. To further clarify the difference in strain gradients for wedge and spherical contacts, see Appendix A. Nevertheless, with all of these differences, hardness invariably decreased with increasing depth for both W and Al single crystals.

These findings would appear to discount existing strain-gradient plasticity models as being applicable to the smallest penetration depths. A search for alternative size effect interpretations should start from a question of how appropriate it is to apply the term "hardness" to a quantity measured at very shallow contact depths. If hardness is understood in terms of resistance to plastic deformation, the condition of a fully plastic regime should be met. It should be stressed that at the earliest stages of indentation, the relative fraction of plastic deformation is small. As follows from TEM observations of indentation induced deformation in Al–0.5wt%Mg and Ni, dislocation structures underneath indentations consisted of a characteristic rosette pattern and a "homogeneous" plastic zone [24]. It was demonstrated that at the earliest stages of the indentation process the extent of rosette arms was much larger than a homogeneous zone radius. A similar conclusion may be drawn from in situ AFM observations on a W single crystal [22]. At this stage, there is a relatively high fraction of elastic material between rosette arms. The authors [24] suggest that the role of elastic deformation in accommodating indentation induced deformation increases with decreasing indentation depth thus resulting in

increasing hardness. With increasing indentation depth, a homogeneous zone radius increases much faster and eventually approaches the extent of the rosette pattern. This was correlated to reaching a depth-independent constant hardness value. Thus, measured values of elevated hardness may reflect the effect of a relatively high contribution of elastic deformation at shallow penetration depths.

With the above, consider that an organization of dislocations in a rosette fashion as opposed to a more homogeneous plastic zone made up of random forest dislocations, has a greater effect on hardness at shallow indentation depths. This would be in keeping with some of our own concepts of inverse pile-up effects [11, 25, 26] and might explain why the *c/a* ratio is in fact larger at smaller depths of penetration [20]. It would be of interest to examine a correlation between hardness and *c/a* for shallow indentation depths. As pointed out above there is no analytical solution available for an elastic/plastic spherical contact. A semi-empirical observation of how (*c/a*) varies with increasing depth allows such a formulation. Data for (*c/a*) from this investigation as well as two previous ones on Fe–3wt%Si [20] and W [9] single crystals are shown as a function of contact radius, *a*, in Fig. 11. It is seen that the single crystal data and finite element data based on Fe–3wt%Si properties give a reasonably tight relationship between *c/a* versus *a* except for one set of tungsten data. An empirical fit is given by

$$\left(\frac{c}{a}\right)^2 = \frac{\eta}{a} \qquad (18)$$

for the rest of the data with η a length scale of 2 μm. Justification for a lower *c/a* cut-off at about 350 nm is based upon *c/a* = 2.33 for the fully-plastic limit. An upper cut-off cannot really be specified as this clearly depends upon the discrete nature of the dislocation process. For example, at the very earliest stages of dislocation activity in aluminum, Tadmor *et al.* [27] show a *c/a* ratio on the order of 10 for a plane-strain wedge. Elsewhere [28] they show a dislocation 350 Å below an 11.6 Å indenter (*c/a*~30) and at yet another loading a Shockley dipole at 42 Å below a spherical contact with a 7 Å radius. These quasi-continuum atomistic simulations demonstrate that the "plasticity" extent depends greatly on the local geometry and type of loading at the contact. We arbitrarily placed a cut-off contact radius at 20 nm since this would represent the smallest depth of penetration (~2 nm) that we could sensibly evaluate with the tips of this investigation. We use this empirical relationship firstly with the contact radius, *a*, as a basis for strain and secondly with the plastic zone, *c*, as a basis.

4.1. "a-Basis" gradients

As given in Table 1, the geometrically-necessary strain measure coupled with the geometry of a spherical contact for small depths ($a^2 \simeq 2\delta R$) leads to

$$\epsilon_p \simeq \frac{a}{4R} \qquad (19)$$

very close to Tabor's estimate. Strictly speaking, however, the plastic displacement associated with the yield excursion is only about half as large as the total displacement. This is seen for both W and NiAl crystals in Figs 6 and 7. While an extreme case for one indent in Fe–3wt%Si did not follow this, most indentations as shown elsewhere [27] did. It was therefore generally the case that $2\delta_{exc} \simeq \delta$. For plastic strain after the excursion, ϵ_{pe}, it follows that $a^2 \simeq 4\delta_{exc}R$ which leads to

$$\epsilon_{pe} \simeq \frac{a}{8R}. \qquad (20)$$

Coupled with the same geometric estimate for contact radius ($a^2 \simeq 2\delta R$), equation (18) yields

$$\left(\frac{c}{a}\right)^2 \simeq \frac{\eta}{(2\delta R)^{1/2}}. \qquad (21)$$

Eliminating *a* through equations (20) and (21) gives plastic strain as a function of penetration depth, tip radius and plastic zone size. For a given depth of penetration, the plastic strain is

$$\epsilon_{pe} \simeq \frac{\sqrt[4]{2\delta R}}{\sqrt{\eta}} \frac{c}{8R}. \qquad (22)$$

and upon differentiation the gradient is

$$\chi_a = \frac{d\epsilon_{pe}}{dc} \simeq \left[\frac{\sqrt{2\delta}}{\eta}\right]^{1/2} \frac{1}{8R^{3/4}}; \quad \eta \simeq 2 \ \mu m \qquad (23)$$

Since the strain was defined on an "*a*-basis" while the gradient is taken with respect to *c*, this involves $d^2\delta/dadc$. Somewhat differently, the "experimental" strains and gradients involved *c* only giving $\chi \simeq d^2\delta_e/dc^2$. When comparing this "experimental" gradient to $\delta^{1/4}/R^{3/4}$ this explains the factor of two difference between the solid curve and the data observed in Fig. 12. One can also compare the gradient predictions of equation (23) to the tungsten data in Fig. 9. The solid curves nearly predict the dependence on tip radius and give an increasing gradient with $\delta^{1/4}$ as might be expected for this somewhat circular argument based on calculated plastic zones and contact radii for tungsten. However, we hasten to add that
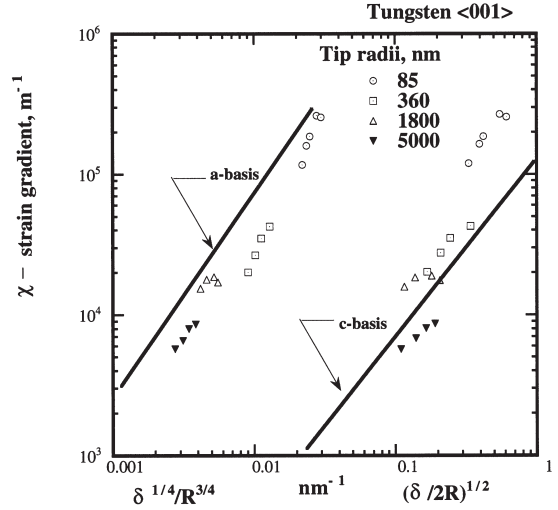

Fig. 12. Strain gradients in tungsten crystals estimated on a contact radius (a) basis or a plastic zone radius (c) basis. Solid curves are comparisons with equations (23) and (25), respectively.

equation (23) also predicts the aluminum data for the two larger tip radii which represent spherical contacts and has utilized measured values of gradients with AFM.

4.2. "c-Basis" gradients

An analogous semi-empirical relation can be determined using the plastic zone as the length-scale basis. Using the same displacement measure,

$$\epsilon_{pe} \simeq \frac{\delta_{exc}}{2c} \qquad (24)$$

Again, using $\delta \simeq 2\delta_{exc}$ and the empirical relationship for c/a given by equation (18), one can show

$$\chi_c = \frac{d\epsilon_{pe}}{dc} \simeq \frac{1}{4\eta}\left(\frac{\delta}{2R}\right)^{1/2}. \qquad (25)$$

This is also shown in Fig. 12 and is seen to conform to much of the data with an underprediction of the data for the sharpest 85 nm radius tip. Comparing equations (23) and (25) it is seen that the difference between χ_a and χ_c, is on the strength of their dependence on the length scale, η, and geometry, δ and R.

4.3. Hardness and the indentation size effect

Using equation (22) as a strain basis for the yield excursion, one can eliminate *c* through equation (17) and define hardness as $P/\pi a^2$, giving

$$\epsilon_{pe} \simeq \frac{3\sqrt{2}}{56\eta} \cdot \frac{\delta^{3/2}}{R^{1/2}} \cdot \frac{H}{\sigma_{ys}}. \tag{26}$$

But ϵ_{pe} is also given by equation (20) and upon elimination with equation (26) gives

$$H \simeq \frac{7\eta}{24\sqrt{2}} \cdot \frac{a^2 \sigma_{ys}}{(R\delta)^{3/2}} \tag{27}$$

Further eliminating a^2 through geometry, this becomes

$$H_a \simeq \frac{7}{12\sqrt{2}} \cdot \frac{\eta \sigma_{ys}}{(\delta R)^{1/2}} \tag{28}$$

Using a "*c*-basis" for strain, one can start with equation (24) and show that with equations (17) and (18)

$$\epsilon_{pe}^2 \simeq \frac{a^3 c^2}{\eta} \cdot \frac{2\pi \sigma_{ys}}{192 R^2 P} \tag{29}$$

Taking hardness as $P/\pi a^2$ and then eliminating ϵ_{pe}^2 through equation (24) gives

$$H = \frac{2ac^2 \sigma_{ys}}{192 R^2 \eta} \cdot \frac{16c^2}{\delta^2} \tag{30}$$

Finally c^4 can be eliminated through equation (18) and a through geometry giving

$$H_c = \frac{\sqrt{2}\eta \sigma_{ys}}{3(\delta R)^{1/2}} \tag{31}$$

This hardness calculated on a "*c*-basis" surprisingly only differs from the "*a*-basis", equation (28), by about 13%. As these are nearly indistinguishable, we show only equation (31) in Fig. 13 where it is seen that the prediction is qualitatively correct but fails quantitatively for the largest tip radius. For the aluminum comparison we invoke $\sigma_{ys}\eta$ in equation (31) to be 300 Pa·m which is about as large as can be justified from Fig. 12 considering a scale factor of 4 μm with a 75 MPa yield strength. The fit appears reasonable in Fig. 14 up to about $[\delta R]^{1/2} \sim 1$ μm. However, for deeper penetration depths with the larger tips, this fails as was observed for the $\langle 001 \rangle$ crystals. This strongly suggests that some factor other than just the contact radius ($\sim [\delta R]^{1/2}$) or perhaps a different functional form of it, is controlling the indentation size effect.

The important point to take away is that there are both experimental data and a semi-empirical rationale in terms of *c/a* that appear to be consistent with an
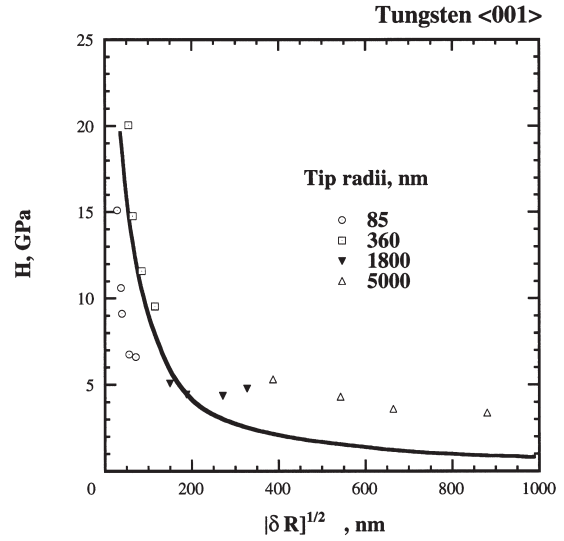

Fig. 13. Hardness as a function of increasing contact radius $(\delta R)^{1/2}$ for spherical contacts into $\langle 100 \rangle$ tungsten compared to equation (31), the solid curve.
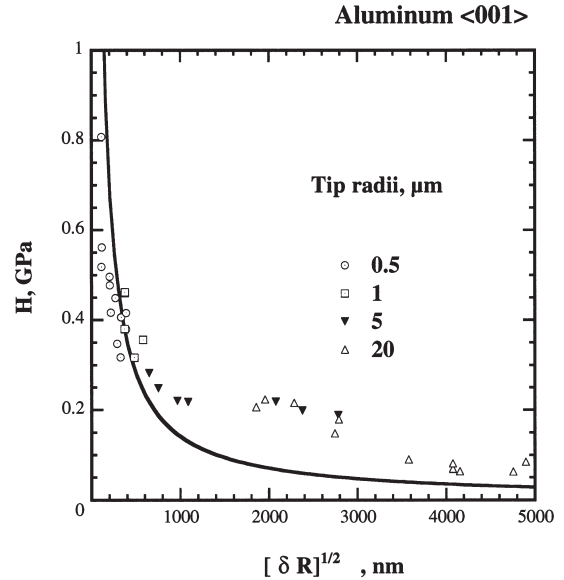

Fig. 14. Hardness as a function of increasing contact radius $(\delta R)^{1/2}$ for spherical contacts into $\langle 100 \rangle$ aluminum compared to equation (31), the solid curve.

indentation size effect. It can be seen that an established empirical relation of $H(c/a)$ agrees satisfactorily with the experimental data. This establishes that the indentation size effect origins may be evaluated by investigating the plastic zone evolution. If further proven, this strongly suggests that different rationale may be needed for different geometries and levels of scale. Here, and as shown in Fig. 9, the strain gradient increases slightly with these spherical indentations at

small penetration depths. For this regime then, spherical tip penetration can result in both an increasing strain gradient and a reduced hardness (the ISE) with increasing depth. See Figs 9 and 14. Part of the physical rationale seems quite simple in that the strain gradient increases because the strain increases with increasing depth of penetration faster than the extent of plasticity increases. While this can occur for curved tips, for the constant strain sharp wedges it does not. The other part of the rationale as to why reduced hardness can coexist with an increasing strain gradient is not intuitive. It is clear from Tables 2 and 3 that the contact area generally increases faster than the strain magnitude. The area increases by nearly a factor of six with deeper penetrations while the strain only increases by a factor of three. While this is also partly explained by a changing c/a ratio, such geometric observations do not offer a good physical basis for explaining the difference between these shallow spherical indentations and deeper constant-angle indentations. One recent suggestion [29] is that the volume to surface area ratio at small indentation depths is important and this is considered in a future paper [29].

5. SUMMARY

Indentation size effects (ISE) for hardness do exist for $\langle 100 \rangle$ single crystals of tungsten and aluminum. Theoretical interpretation of strain gradients (χ) suggest a depth (δ) independence for χ with spherical tips and a $1/\delta$ dependence for perfectly sharp wedges. From semi-empirical analysis and observations of the plastic zone to contact radius ratio, c/a, it is proposed that strain gradients increase somewhat with depth for spherical tips. This opposite tendency for strain gradient (spheres vs wedges) is supported by both tungsten and aluminum single crystal observations. Both crystal types, however, exhibit an ISE irrespective of the trend in their gradients. As hardness decreases more like $1/[\delta R]^{1/2}$, in agreement with the semi-empirical observations of c/a, alternative explanations to the strain gradient plasticity arguments seem to be required for shallow indentations with spherical tips.

REFERENCES

1. Stelmashenko, N. A., Walls, N. G., Brown, L. M. and Milman, Y. V., *Acta metall. mater.*, 1993, **41**, 2855.
2. Ma, Q. and Clarke, D. R., *J. Mater. Res.*, 1995, **10**, 853.
3. Nix, W. D. and Gao, H., *J. Mech. Phys. Solids*, 1998, **46**(3), 411.
4. Tabor, D., *Hardness of Metals*. Oxford University Press, Oxford, 1951.
5. Venkataraman, S.K., PhD Dissertation, University of Minnesota, 1994.
6. Pethica, J. B., Hutchings, R. and Oliver, W. C., *Phil. Mag. A*, 1983, **48**, 539.
7. Oliver, W. C. and Pharr, G. M., *J. Mater. Res.*, 1992, **7**, 1564.
8. Syed Asif, S. A. and Pethica, J. B., *Phil. Mag. A*, 1987, **76**, 1105.
9. Bahr, D. F., Kramer, D. E. and Gerberich, W. W., *Acta mater.*, 1998, **46**, 3605.
10. Mann, A. B. and Pethica, J. B., *Phil. Mag. A*, 1999, **79**, 577.
11. Gerberich, W. W., Kramer, D. E., Tymiak, N. I., Volinsky, A. A., Bahr, D. F. and Kriese, M. D., *Acta mater.*, 1999, **47**(15), 4115.
12. Corcoran, S. G., Colton, R. J., Lilleodden, E. T. and Gerberich, W. W., *Phys. Rev. B*, 1997, **55**, R16057.
13. Michalske, T. A. and Houston, J. E., *Acta mater.*, 1998, **46**, 391.
14. Kiely, J. D. and Houston, J. E., *Phys. Rev. B*, 1998, **57**, 12588.
15. Gouldstone, A., Koh, H. -J., Zeng, K. -Y., Giannako-poulos, A. E. and Suresh, S., *Acta mater.*, 2000, **48**, 2277.
16. Lucas, B. N. and Oliver, W. C., *Mat. Res. Soc. Proc.*, 1992, **239**, 337.
17. Stone, D., LaFontaine, W. R., Alexopolous, P., Wu, T. -W. and Li, C. Y., *J. Mater. Res.*, 1988, **3**, 141.
18. Matthews, J. R., *Acta mater.*, 1980, **28**, 311.
19. Mulhearn, T. O., *J. Mech. Phys. Solids*, 1959, **7**, 85.
20. Harvey, S., Huang, H., Venkataraman, S. and Gerberich, W. W., *J. Mater. Res.*, 1993, **8**(6), 1291.
21. Kramer, D. E., Huang, H., Kriese, M., Robach, J., Nelson, J., Wright, A., Bahr, D. and Gerberich, W. W., *Acta mater.*, 1999, **47**(1), 333.
22. Johnson, K. L., *J. Mech. Phys. Solids*, 1970, **18**, 115.
23. Kramer, D. E., Yoder, D. B. and Gerberich, W. W., *Phil. Mag.*, accepted for publication, 2001.
24. Yasuda, K., Shinohara, K., Kinoshita, C. and Arai, M., in *Proc. 10th Int. Conf. Japan Inst. Metals, Sendai, Japan*, 1994, p. 865.
25. Gerberich, W. W., Venkataraman, S. K., Huang, H., Harvey, S. E. and Kohlstedt, D. L., *Acta metall. mater.*, 1995, **43**(4), 1569.
26. Gerberich, W. W., Nelson, J. C., Lilleodden, E. T., Anderson, P. and Wyrobek, J. T., *Acta mater.*, 1996, **44**(9), 3585.
27. Tadmor, E. B., Miller, R., Phillips, R. and Ortiz, M., *J. Mater. Res.*, 1999, **14**, 2233.
28. Phillips, R., Rodney, D., Shenoy, V., Tadmor, E. and Ortiz, M., *Modelling Simul. Mater. Sci. Eng.*, 1999, **7**, 769.
29. Baskes, M., Los Alamos National Laboratories, 2000, private communication.

APPENDIX A

The following establishes a correlation between a definition of plastic gradient as used in this paper and plastic gradient defined as a spatial variation of plastic strain. Consider a radial distribution of plastic strain $\epsilon_p(r)$ starting from an indenter surface ($r = 0$) up to an elastic–plastic boundary ($r = c$). Within these boundaries, plastic strain decreases from its maximum value $\epsilon_p(0)$ to zero. The most crude estimate of $\epsilon_p(r)$ would be a linear dependence as shown in Fig. A1. This is used for pedagogical purposes to qualitatively illustrate the differences between sharp wedge and spherical contacts. For such a plastic strain distribution, the plastic strain gradient,
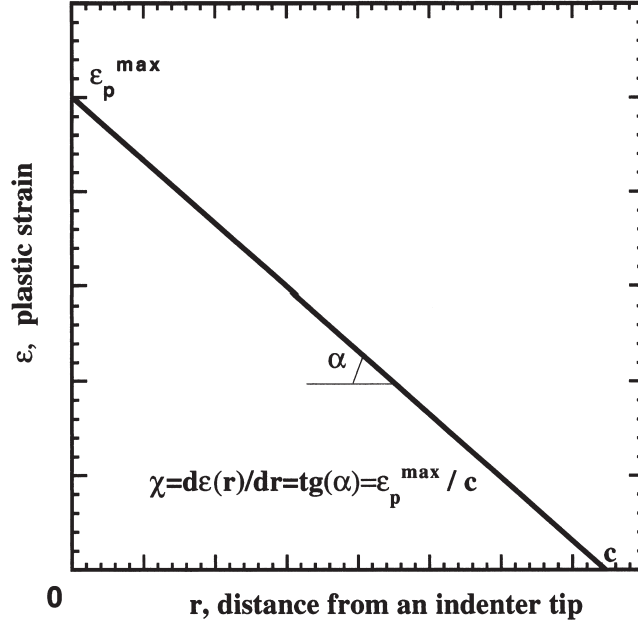
Fig. A1. A schematic of plastic strain distribution within an indentation induced plastic zone. A linear plastic strain distribution is assumed.
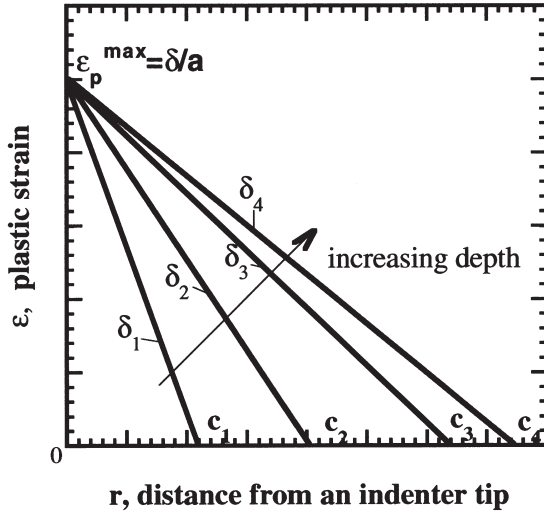

Fig. A2. Plastic strain distribution under a sharp wedge contact. Each line corresponds to a different indentation depth.
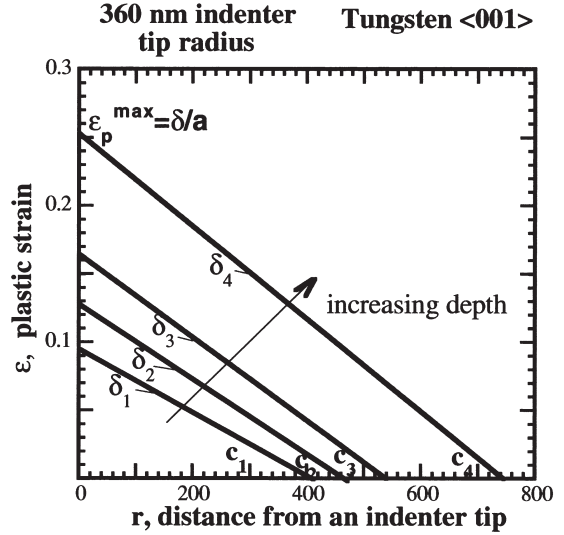

Fig. A3. Plastic strain distribution under a spherical contact. Each line corresponds to a different indentation depth.

$$\chi = \frac{d\epsilon_p(r)}{dr}$$

simply equals the slope of this line

$$\tan\alpha = \frac{e_p^{max}}{c}.$$

Thus, both definitions of plastic strain gradient are equivalent in this case. Assuming the plastic strain distribution shown in Fig. A1, we can visualize the difference between $\chi(\delta)$ trends for spherical and wedge contacts. In both cases, consider indentation depths $\delta_1 < \delta_2 < \delta_3 < \delta_4$ with the corresponding plastic zones $c_1 < c_2 < c_3 < c_4$ and assume

$$\epsilon_p^{max} = \frac{\delta}{a}.$$

A.1. Wedge contact

For a wedge with an included angle $\theta, \epsilon_p^1 = \epsilon_p^2 = \epsilon_p^3 = \epsilon_p^4 = \tan\theta$ but $c_1 < c_2 < c_3 < c_4$ so it is clear that $\tan\alpha_1 > \tan\alpha_2 > \tan\alpha_3 > \tan\alpha_4$ as seen in Fig. 16. Consequently, $\chi_1 > \chi_2 > \chi_3 > \chi_4$.

A.2. Spherical contact

For a spherical contact, both $c_1 < c_2 < c_3 < c_4$ and $\epsilon_p^1 < \epsilon_p^2 < \epsilon_p^3 < \epsilon_p^4$. In this case, experimental values of indentation depths and corresponding plastic zone radii are required to evaluate $\chi(\delta)$ trends. For this purpose, we utilized tungsten single crystal data for a 360 nm indenter tip. Results presented in Fig. A3 indicate slopes increasing with the increasing indentation depths and, consequently $\chi_1 < \chi_2 < \chi_3 < \chi_4$.